

## Ptychographic atomic electron tomography: Towards three-dimensional imaging of individual light atoms in materials

Dillan J. Chang <sup>1</sup>, Dennis S. Kim <sup>1</sup>, Arjun Rana,<sup>1</sup> Xuezheng Tian,<sup>1</sup> Jihan Zhou,<sup>1</sup> Peter Ercius <sup>2</sup>, and Jianwei Miao <sup>1</sup>

<sup>1</sup>*Department of Physics & Astronomy and California NanoSystems Institute, University of California, Los Angeles, California 90095, USA*

<sup>2</sup>*National Center for Electron Microscopy, Molecular Foundry, Lawrence Berkeley National Laboratory, Berkeley, California 94720, USA*

 (Received 3 May 2020; revised 10 September 2020; accepted 20 October 2020; published 2 November 2020)

Through numerical simulations, we demonstrate the combination of ptychography and atomic electron tomography as an effective method for low dose imaging of individual low-Z atoms in three dimensions. After generating noisy diffraction patterns with multislice simulations of an aberration-corrected scanning transmission electron microscope through a 5-nm zinc-oxide nanoparticle, we have achieved three-dimensional (3D) imaging of individual zinc and oxygen atoms and their defects by performing tomography on ptychographic projections. The methodology has also been simulated in 2D materials, resolving individual sulfur atoms in vertical WS<sub>2</sub>/WSe<sub>2</sub> van der Waals heterostructure with a low total electron dose where annular-dark-field images fail to resolve. We envision that the development of this method could be instrumental in studying the precise 3D atomic structures of radiation sensitive systems and low-Z atomic structures such as 2D heterostructures, catalysts, functional oxides, and glasses.

DOI: [10.1103/PhysRevB.102.174101](https://doi.org/10.1103/PhysRevB.102.174101)

Atomic electron tomography (AET) determines three-dimensional (3D) coordinates of individual atoms in materials without assuming crystallinity by combining high-resolution tomographic tilt series from scanning transmission electron microscopes (STEM) with powerful iterative tomographic algorithms [1]. Since its inception, AET has successfully imaged grain boundaries, dislocations, point defects, bond distortion, strain tensors, chemical order/disorder, and nucleation dynamics with high 3D precision [2–10]. More recently, the method has been extended to 2D materials to locate individual atoms in transition metal dichalcogenides with picometer precision and correlate dopant induced local strain to electronic band structures [10].

However, all projection measurements in AET so far have been limited to *incoherent* electron-scattering methods such as (high angle) annular dark field (ADF/HAADF) [11–13], whereas imaging methods from *coherent* beam sources have made significant strides in recent decades [14–17]. One of these is ptychography, a powerful scanning coherent diffractive imaging method that can solve for both the amplitude and phase of the specimen and probe by exploiting sufficient redundancies from overlapped probes and using iterative algorithms [14,18,19]. Although ptychography was proposed in 1969 [20] and realized with STEM to image crystalline silicon past the conventional information limit [21], the modern version of ptychography using iterative algorithms to retrieve the magnitude and phase of noncrystalline objects was demonstrated with x rays in 2017 [18], which was based on a coherent diffractive imaging experiment in 1999 [22]. Ptychography has since been broadly applied to image a wide range of physical and biological specimens in two and three

dimensions using x rays, electrons, high harmonic generation, and optical lasers [23–33].

Conventionally, ptychography is an imaging method in two dimensions, but it has also been extended to recover 3D information from a single projection by modeling the object as multiple slices of phase objects [34,35]. However, the depth resolution of this method is limited by  $D_{\text{dep}} = \frac{\lambda}{2\sin^2(\frac{\theta_{\text{max}}}{2})}$  compared to the transverse resolution limitation of  $D_{\text{tran}} = \frac{\lambda}{\sin(\theta_{\text{max}})}$ , where  $\lambda$  is the wavelength of the probe and  $\theta_{\text{max}}$  is the maximum detector collection angle [34,36]. As an example, a STEM experiment with an 80-keV electron probe and 80-mrad maximum collection angle would yield a theoretical maximum depth resolution of 1.3 nm compared to its transverse counterpart of 0.39 Å. Since atomic resolution typically requires near-angstrom resolution, single-projection multislice ptychography alone would not be able to recover signals from individual atoms in three dimensions. Due to this limitation, ptychographic data have to be measured at multiple tilt angles and combined with tomography to achieve high depth resolution in 3D phase images [23,33,34]. As powerful single-electron pixel-array detectors that can achieve deep subangstrom resolution [37,38] become commercially available, ptychographic AET (pAET) has evolved from a hypothetical idea to an experimental possibility. In this paper, we use numerical experiments to demonstrate pAET as a feasible method for low-dose 3D imaging of individual light atoms by performing multislice simulations on a zinc-oxide nanoparticle and a vertical WS<sub>2</sub>/WSe<sub>2</sub> van der Waals (vdW) heterostructure.

An atomic model of a spherical Wurtzite ZnO nanoparticle with a diameter of 5 nm was generated with 1% randomly

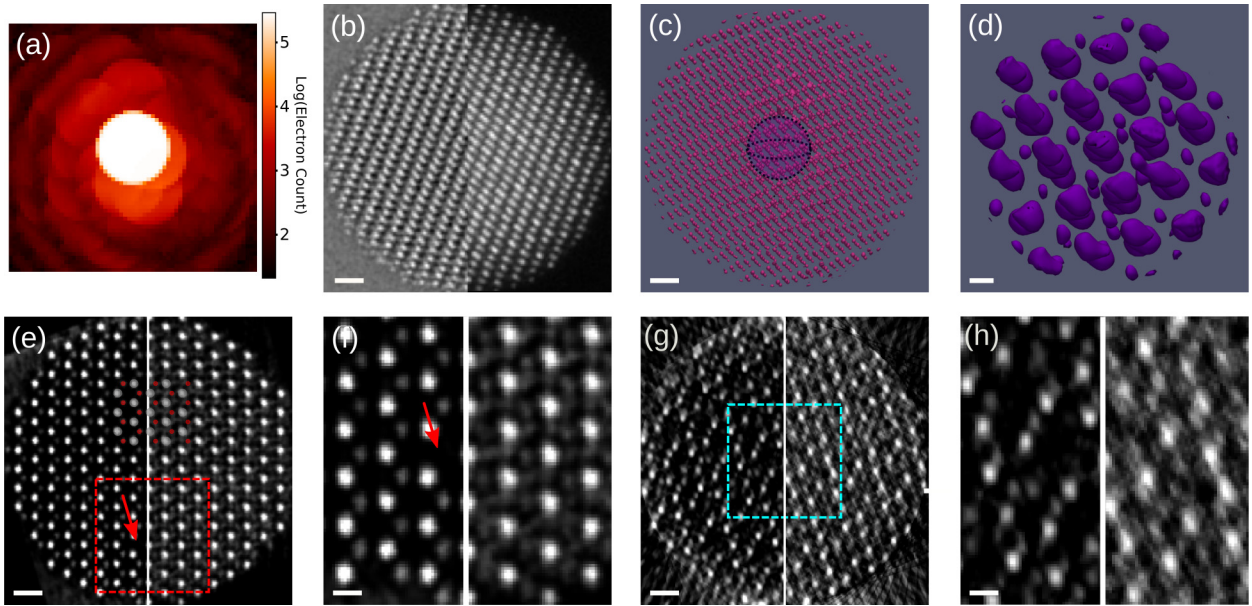


FIG. 1. Numerical experiment on ptychography- and ADF-STEM-based atomic electron tomography of a 5-nm ZnO nanoparticle. (a) 2D logarithmic heat map of the average of 15 625 diffraction patterns from a tilt series. The diffraction patterns simulate a dose per projection of  $3.0 \times 10^4 e/\text{\AA}^2$ . (b) A representative ptychographic phase projection (left) and an ADF-STEM projection (right). Both projections were reconstructed with the same diffraction patterns seen in (a). (c) 3D isosurface rendering of the volume after tomographic reconstruction of ptychographic phase projections. (d) Magnified isosurface rendering of the core of the volume in (c). Individual oxygen atoms rendered as smaller spheres are observed. Note that the zinc atoms look disproportionately large due to the isosurface rendering effect. (e) A 2.0-Å-thick central slice of the volume in the [0001] direction reconstructed with ptychographic phase projections (left) and with ADF-STEM projections (right). (f) A magnified image of (e), indicating an oxygen defect with a red arrow. (g) A 2.0-Å-thick slice through the missing wedge direction of the reconstruction performed with ptychographic projections (left) and with ADF projections (right). (h) A magnified image of (g), demonstrating greater missing wedge artifacts in the reconstruction when performing tomography with ADF-STEM projections. Scale bars in (b), (c), (e), and (g) indicate 5 Å, scale bar in (d) indicates 1 Å, and scale bars in (f) and (h) indicate 2 Å.

dispersed oxygen vacancies. This model was used to generate 0.2-Å-thick projected potential slices for multislice simulation (probe sampling: 0.1 Å; sample sampling: 0.1 Å; maximum detector angle: 104 mrad) [39,40] using tabulated Hartree-Fock approximations of atomic potentials [41,42]. An aberration-corrected STEM probe was simulated using the parameters of the TEAM 0.5 (electron energy: 80 keV; probe semiconvergence angle: 30 mrad; C1: 0 nm; C3: 900 nm; C5:  $-622 \mu\text{m}$ ; probe size: 0.88 Å; probe step size: 0.4 Å). By tilting the ZnO nanoparticle from  $-70^\circ$  to  $+70^\circ$ , we calculated 29 data sets of diffraction patterns at 29 tilt angles. For each tilt angle, eight frozen phonon configurations at room temperature were obtained and averaged for the data set. Unlike conventional AET tilt series where each tilt image is a 2D ADF or HAADF image, a ptychographic tilt series consists of 4D data sets: two dimensions from scanning the sample in real space, and two from the diffraction in momentum space. To represent real experimental conditions, the 4D data sets were corrupted with simulated Poisson noise by sampling independent electron events from the ideal diffraction patterns. The diffraction patterns were sampled to represent an effective dose per projection of  $3.0 \times 10^4 e/\text{\AA}^2$ , thus simulating a total electron radiation dose of  $8.7 \times 10^5 e/\text{\AA}^2$ . Figure 1(a) shows a 2D logarithmic heat map of the average diffraction pattern from one tilt series projection.

The overlap of adjacent probes (44%) gives enough redundancy to iteratively solve for both object and probe

functions using the extended ptychographic iterative engine (ePIE) algorithm [43]. Due to high Poisson noise in individual diffraction patterns, we used a small update parameter (0.01) for the object function to prevent overfitting the noise in reconstructions. Figure 1(b) shows an example of a ptychographic phase reconstruction on the left-hand side, and the ADF image (detector inner angle: 30 mrad; outer angle: 90 mrad) generated from the same diffraction data set on the right-hand side. 3D reconstructions of both ptychographic and ADF projections were performed using REal Space Iterative Reconstruction (RESIRE)—a powerful tomographic algorithm that iteratively minimizes the error between the measured and calculated projections using the gradient descent [44]. Isosurface rendering of the 3D reconstruction performed with ptychographic projections are shown in Fig. 1(c), with a magnified isosurface rendering of the volume's core in Fig. 1(d). 3D rendering of individual oxygen atoms can be observed in the magnified figure. Figure 1(e) shows 2.0-Å-thick central slice of the 3D volume reconstructed with ptychographic phase projections on the left-hand side, and with ADF-STEM projections on the right-hand side, with a magnified image shown in Fig. 1(f). The smaller blobs found in the ePIE/RESIRE reconstruction correspond to individual oxygen atoms, which were not resolved using ADF/RESIRE. Because RESIRE does not assume any periodicity while performing 3D reconstruction, individual oxygen atom defects placed in the original model were also able to

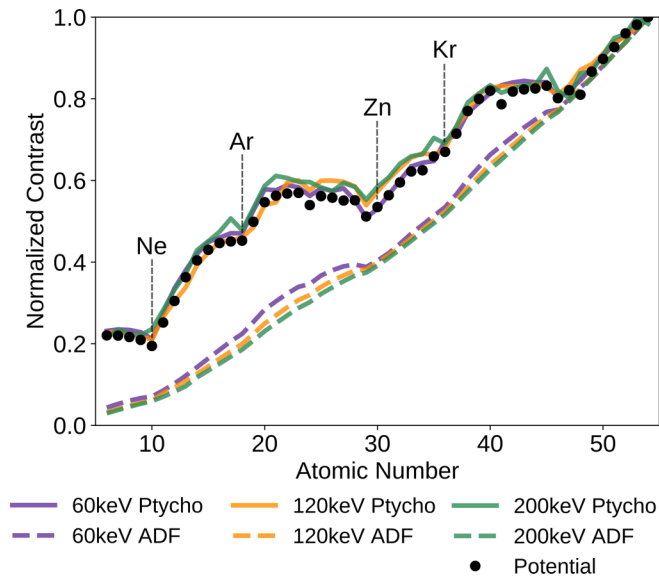


FIG. 2. Quantitative comparison of normalized atomic contrast from C to Xe between ptychography and ADF for three different electron beam energies (60, 120, and 240 keV). Normalized peak heights from Hartree-Fock potential estimations are also plotted. Atoms where valence shells become fully filled (Ne, Ar, Zn, and Kr) are indicated to explain fluctuations in the potential peaks.

be resolved in the pAET reconstruction as indicated by the red arrow in Fig. 1(f). Furthermore, the improved quality in pAET reconstructions is especially evident when looking at a slice through the missing wedge direction, shown in Fig. 1(g), and magnified in Fig. 1(h).

To better understand the nature of individual low-Z atom contrast with pAET, we performed multislice simulations of individual atoms with varying atomic number to measure their relative contrast. Similar calculations have been performed analytically for phase contrast [45], and numerically for ADF-STEM and bright field STEM contrast [41]. Multislice simulations of individual atoms ranging from C ( $Z = 6$ ) to Xe ( $Z = 54$ ) were performed with an aberration-corrected probe (semiconvergence angle: 24 mrad) of varying energies (60, 120, and 200 keV) and probe step size of 0.4 Å. Ptychographic phase projections were reconstructed with ePIE and ADF-STEM projections were reconstructed by integrating the diffraction patterns from 24 to 120 mrad. Contrast per atom was defined as the height of the fitted 2D Gaussian function and were normalized by setting the atomic contrast of Xe to unity. Finally, projected atomic potentials were calculated and fitted as 2D Gaussians to measure ideal relative atomic contrasts. The results of these calculations are shown in Fig. 2. Note that the contrasts from the potentials are not strictly monotonic as a function of atomic number, as variations in the filling of electron shells create fluctuations reflected by the Hartree-Fock approximations. We found that the contrast from ADF-STEM was monotonic as a function of the atomic number, supporting previous studies that report a power relation (roughly proportional to  $Z^{1.8}$ ) [11–13]. Such a relation can be tolerated while conducting tomography in metallic samples, but this makes it more difficult to simultaneously image individual low- and high-Z atoms, such as in metallic oxides,

due to a large ratio of the relative signal ( $S_{Zn}/S_O = 7.75$ ). In contrast, ptychography was not only able to recover a higher relative signal for low-Z atoms compared to ADF-STEM ( $S_{Zn}/S_O = 2.48$ ), but also was sensitive enough to recover the aforementioned fluctuations in atomic potentials for all three beam energies. This advantage of using phase signals for tomography has also been numerically demonstrated with multislice simulation of high-resolution transmission-electron microscopy images as input projections [46].

Successful tomography requires that the input projections need to be a sum of some monotonic response to a physical property along the direction of projection—a requirement aptly named as the *projection requirement* [11,47]. Although perfect linearity is ideal, power-law atomic contrast in ADF/HAADF-STEM projections is sufficient to locate and identify individual atoms in materials, but it requires a relatively high electron dose [1–10]. In contrast, ptychography reconstructs the phase induced in the transmitted beam by the Coulomb potential, which acts as a linear response to atoms. Therefore, we should expect a higher degree of linearity in AET projections reconstructed with ptychography. Figure 3(a) shows the graphical representation of the multislice simulation used to test linearity in ADF/HAADF-STEM images.  $N$  Si atoms separated by a distance  $d = 3$  Å were placed colinearly in the path of the electron beam (energy: 80 keV; semiconvergence angle  $\alpha$ : 24 mrad), and was sampled with a probe step size of 0.4 Å. Three different projections of atomic columns were calculated using five different inner and outer ADF detector angle combinations. After fitting each projection of atom columns to a 2D Gaussian, the contrast per atom was measured as the height of the 2D Gaussian divided by the number of atoms. The result of this calculation is shown in Fig. 3(b), along with a horizontal line at 1 indicating contrast per atom from ideal linear projections. We observed significant deviation from the linear contrast when the collection angles were smaller than  $6\alpha$  as channeling effects due to low electron beam energy distorted the images of columns. Furthermore, the measured atomic contrast was highly sensitive to the collection angles in this regime due to multiple scattering. Only when the measured inner angle was higher than  $6\alpha$  did we observe monotonicity in the contrast per atom. This might suggest HAADF-STEM as a more suitable method than ADF-STEM when performing AET using low-energy beams, but the electron dose in real HAADF-STEM experiments required to sufficiently overcome Poisson noise makes it a less reliable choice when imaging dose sensitive materials. For a comparison, we performed a similar numerical experiment by replacing the ADF detector with a pixel array detector for ptychography, shown in Fig. 3(c), and plotted results from contrast calculations in Fig. 3(d). Ptychography was able to maintain a more linear contrast per atom than ADF/HAADF-STEM.

Last, the method of pAET can also be used to image individual low-Z atoms in geometries other than nanoparticles such as thin films and vdW heterostructures. The vdW interaction between the top and bottom layers mediates various types of coupling across the interface in vdW heterostructures. It has been reported that the quantum properties of vdW heterostructures are highly tunable with vertical stacking through moiré potentials, and that different stacking align-

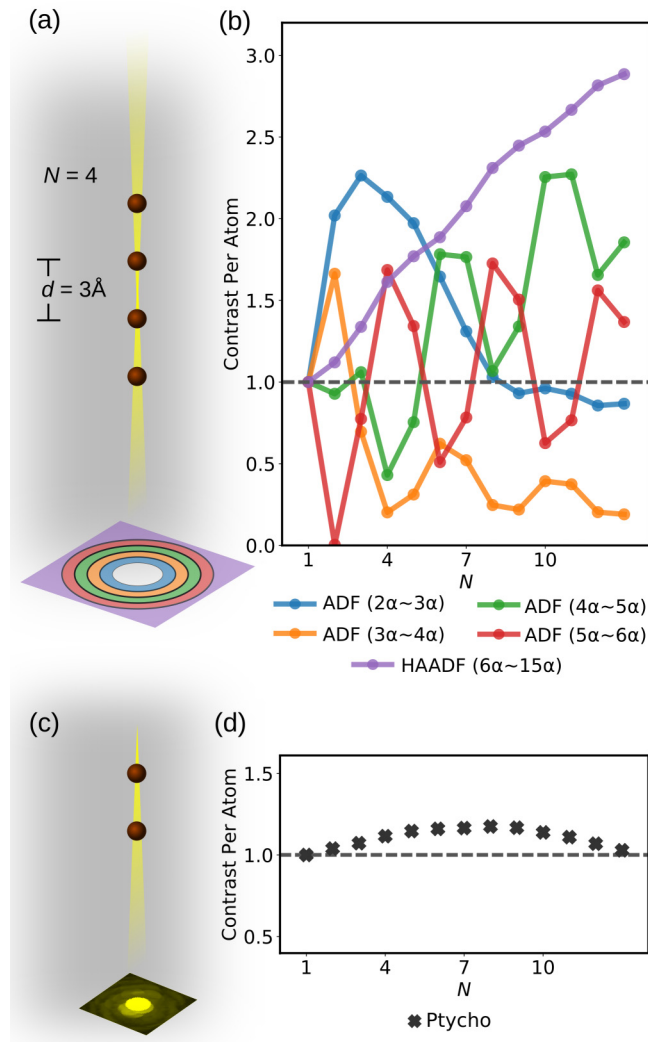


FIG. 3. Contrast per atom when imaging along the zone axis with ADF/HAADF and ptychography. (a) An experimental schematic of multislice simulation of an 80-keV electron beam probe and 24-mrad semi-convergence angle imaging a column of  $N$  Si atoms separated by distance of 3 Å. Five different combinations of inner and outer angles were simulated. (b) Contrast per atom in atomic columns when measured with various ADF angles. The horizontal gray line plotted at 1 indicates the ideal linear projection. (c) Similar experimental schematic as (a) except the substitution of ADF detectors with a pixel array detector, allowing for ptychographic reconstruction. (d) Contrast per atom in columns when reconstructed with ptychography.

ments can cause drastic changes in exciton excitation as well as other quantum properties such as superconductivity and correlated insulator states [48–52]. The capability to precisely determine the 3D coordinates and chemical species of individual atoms combined with *ab initio* calculations is anticipated to reveal unprecedented details about the correlation between the atomic structure of vdW heterostructures and their exotic quantum properties. Using identical electron probe parameters as those used in Fig. 1, multislice simulation was performed on an atomic model of vertical  $\text{WS}_2/\text{WSe}_2$  van der Waals heterostructure, with its two tungsten layers separated by 6.54 Å and tiled by 12.5°. Figure 4(a) shows

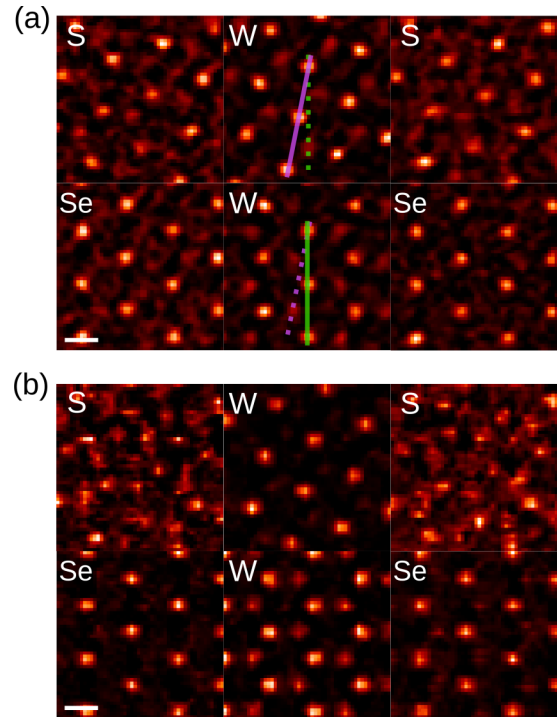


FIG. 4. Numerical experiment on ptychography- and ADF-STEM-based AET of a vertical  $\text{WS}_2/\text{WSe}_2$  van der Waals heterostructure. (a) 2.0-Å-thick slices of each atomic layer when simulated with a total electron dose of  $5.1 \times 10^4 e/\text{Å}^2$  and reconstructed with ePIE and RESIRE. Tilt angle of 12.5° between the two tungsten layers was recovered, indicated by colored lines. (b) 2.0-Å-thick slices of the same experiment as (a) when reconstructed with ADF and RESIRE. Scale bars, 2 Å.

2.0-Å-thick slices of every atomic layer of the heterostructure when reconstructed with ePIE and RESIRE. Despite severely corrupting the diffraction patterns by simulating a total electron dose of  $5.1 \times 10^4 e/\text{Å}^2$ , every atomic layer including the two sulfur layers are resolved. However, when tomography was performed on ADF-STEM projections with an equivalent electron dose, as shown in Fig. 4(b), the signals from the sulfur layers attenuate below a level at which individual atoms are traceable.

In summary, by leveraging improved signal from low- $Z$  atoms and linearity in atomic projections, ptychographic reconstructions from 4D-STEM data can offer significant advantages when performing electron tomography at the atomic scale. To demonstrate these advantages, we simulated a ptychographic tomography tilt series of 29 projections of a 5-nm Wurtzite zinc-oxide nanoparticle using the multislice simulation, reconstructed each projection using ePIE, and performed tomography with RESIRE to resolve individual oxygen atoms and their defects. We also believe that pAET serves as a possible alternative to conventional AET methods for low dose 3D atomic imaging of 2D materials. After simulating pAET on vertical  $\text{WS}_2/\text{WSe}_2$  van der Waals heterostructure with a low electron dose of  $5.1 \times 10^4 e/\text{Å}^2$ , we were able to resolve every layer including the lightest sulfur layer to the atomic resolution. As high quality pixel array electron detectors become more commercially viable and data storage and management

become more streamlined, we envision pAET as a powerful method for studying the 3D atomic structures of low- $Z$  and radiation sensitive materials such as transition metal oxides, functional 2D heterostructures, and glasses.

We thank M. Pham and Y. Yuan for sharing with us the RESIRE code. This work was primarily supported by the U.S. Department of Energy (DOE), Office of Science, Basic Energy Sciences (BES), Division of Materials Sciences and Engineering under Award No. DE-SC0010378. We also

acknowledge the support by STROBE: A National Science Foundation Science & Technology Center under Grant No. DMR 1548924, an Army Research Office MURI grant on Ab-Initio Solid-State Quantum Materials: Design, Production and Characterization at the Atomic Scale (AFOSR Grant No. W911NF1810432) and the NSF DMREF program (Grant No. DMR-1437263). We acknowledge support from the Molecular Foundry, Lawrence Berkeley National Laboratory, which is supported by the U.S. Department of Energy under Contract No. DE-AC02-05CH11231.

- 
- [1] J. Miao, P. Ercius, and S. J. L. Billinge, *Science* **353**, aaf2157 (2016).
- [2] M. C. Scott, C.-C. Chen, M. Mecklenburg, C. Zhu, R. Xu, P. Ercius, U. Dahmen, B. C. Regan, and J. Miao, *Nature (London)* **483**, 444 (2012).
- [3] C.-C. Chen, C. Zhu, E. R. White, C.-Y. Chiu, M. C. Scott, B. C. Regan, L. D. Marks, Y. Huang, and J. Miao, *Nature (London)* **496**, 74 (2013).
- [4] B. Goris, A. De Backer, S. Van Aert, S. Gómez-Graña, L. M. Liz-Marzán, G. Van Tendeloo, and S. Bals, *Nano Lett.* **13**, 4236 (2013).
- [5] R. Xu *et al.*, *Nat. Mater.* **14**, 1099 (2015).
- [6] G. Haberfehlner, P. Thaler, D. Knez, A. Volk, F. Hofer, W. E. Ernst, and G. Kothleitner, *Nat. Commun.* **6**, 8779 (2015).
- [7] Y. Yang *et al.*, *Nature (London)* **542**, 75 (2017).
- [8] J. Zhou *et al.*, *Nature (London)* **570**, 500 (2019).
- [9] J. Zhou, Y. Yang, P. Ercius, and J. Miao, *MRS Bull.* **45**, 290 (2020).
- [10] X. Tian *et al.*, *Nat. Mater.* **19**, 867 (2020).
- [11] P. A. Midgley and M. Weyland, *Ultramicroscopy* **96**, 413 (2003).
- [12] J. M. LeBeau, S. D. Findlay, L. J. Allen, and S. Stemmer, *Phys. Rev. Lett.* **100**, 206101 (2008).
- [13] S. J. Pennycook and P. D. Nellist, editors, *Scanning Transmission Electron Microscopy* (Springer, New York, 2011).
- [14] J. Miao, T. Ishikawa, I. K. Robinson, and M. Murnane, *Science* **348**, 530 (2015).
- [15] J. Miao, T. Ohsuna, O. Terasaki, K. O. Hodgson, and M. A. O’Keefe, *Phys. Rev. Lett.* **89**, 155502 (2002).
- [16] J. M. Zuo, I. Vartanyants, M. Gao, R. Zhang, and L. A. Nagahara, *Science* **300**, 1419 (2003).
- [17] L. De Caro, E. Carlino, G. Caputo, P. D. Cozzoli, and C. Giannini, *Nat. Nanotechnol.* **5**, 360 (2010).
- [18] J. M. Rodenburg, A. C. Hurst, A. G. Cullis, B. R. Dobson, F. Pfeiffer, O. Bunk, C. David, K. Jefimovs, and I. Johnson, *Phys. Rev. Lett.* **98**, 034801 (2007).
- [19] P. Thibault, M. Dierolf, A. Menzel, O. Bunk, C. David, and F. Pfeiffer, *Science* **321**, 379 (2008).
- [20] W. Hoppe, *Acta Crystallogr., Sect. A* **25**, 495 (1969).
- [21] P. D. Nellist, B. C. McCallum, and J. M. Rodenburg, *Nature (London)* **374**, 630 (1995).
- [22] J. Miao, P. Charalambous, J. Kirz, and D. Sayre, *Nature (London)* **400**, 342 (1999).
- [23] M. Dierolf, A. Menzel, P. Thibault, P. Schneider, C. M. Kewish, R. Wepf, O. Bunk, and F. Pfeiffer, *Nature (London)* **467**, 436 (2010).
- [24] M. J. Humphry, B. Kraus, A. C. Hurst, A. M. Maiden, and J. M. Rodenburg, *Nat. Commun.* **3**, 730 (2012).
- [25] G. Zheng, R. Horstmeyer, and C. Yang, *Nat. Photonics* **7**, 739 (2013).
- [26] D. A. Shapiro *et al.*, *Nat. Photonics* **8**, 765 (2014).
- [27] H. Yang *et al.*, *Nat. Commun.* **7**, 12532 (2016).
- [28] M. Holler, M. Guizar-Sicairos, E. H. Tsai, R. Dinapoli, E. Müller, O. Bunk, J. Raabe, and G. Aeppli, *Nature (London)* **543**, 402 (2017).
- [29] C. Donnelly, M. Guizar-Sicairos, V. Scagnoli, S. Gliga, M. Holler, J. Raabe, and L. J. Heyderman, *Nature (London)* **547**, 328 (2017).
- [30] S. Gao, P. Wang, F. Zhang, G. T. Martinez, P. D. Nellist, X. Pan, and A. I. Kirkland, *Nat. Commun.* **8**, 163 (2017).
- [31] P. Wang, F. Zhang, S. Gao, M. Zhang, and A. I. Kirkland, *Sci. Rep.* **7**, 2857 (2017).
- [32] J. Deng *et al.*, *Sci. Adv.* **4**, eaau4548 (2018).
- [33] P. Li and A. Maiden, *Sci. Rep.* **8**, 2049 (2018).
- [34] K. S. Raines, S. Salha, R. L. Sandberg, H. Jiang, J. A. Rodriguez, B. P. Fahimian, H. C. Kapteyn, J. Du, and J. Miao, *Nature (London)* **463**, 214 (2010).
- [35] A. M. Maiden, M. J. Humphry, and J. M. Rodenburg, *J. Opt. Soc. Am. A* **29**, 1606 (2012).
- [36] A. Suzuki, S. Furutaku, K. Shimomura, K. Yamauchi, Y. Kohmura, T. Ishikawa, and Y. Takahashi, *Phys. Rev. Lett.* **112**, 053903 (2014).
- [37] Y. Jiang *et al.*, *Nature (London)* **559**, 343 (2018).
- [38] Z. Chen, M. Odstreil, Y. Jiang, Y. Han, M.-H. Chiu, L.-J. Li, and D. A. Muller, *Nat. Commun.* **11**, 2994 (2020).
- [39] J. M. Cowley and A. F. Moodie, *Acta Crystallogr.* **10**, 609 (1957).
- [40] E. J. Kirkland, R. F. Loane, and J. Silcox, *Ultramicroscopy* **23**, 77 (1987).
- [41] E. J. Kirkland, *Advanced Computing in Electron Microscopy* (Springer, Boston, MA, 2010).
- [42] A. Pryor, Y. Yang, A. Rana, M. Gallagher-Jones, J. Zhou, Y. H. Lo, G. Melinte, W. Chiu, J. A. Rodriguez, and J. Miao, *Sci. Rep.* **7**, 10409 (2017).
- [43] A. M. Maiden and J. M. Rodenburg, *Ultramicroscopy* **109**, 1256 (2009).
- [44] Y. Yao *et al.*, [arXiv:2004.02266](https://arxiv.org/abs/2004.02266).
- [45] C. B. Eisenhandler and B. M. Siegel, *J. Appl. Phys.* **37**, 1613 (1966).
- [46] D. Ren, C. Ophus, M. Chen, and L. Waller, *Ultramicroscopy* **208**, 112860 (2020).

- [47] P. W. Hawkes, in *Electron Tomography*, edited by J. Frank (Springer, Boston, MA, 1992), pp.17–38.
- [48] C. Zhang, C.-P. Chuu, X. Ren, M.-Y. Li, L.-J. Li, C. Jin, M.-Y. Chou, and C.-K. Shih, *Sci. Adv.* **3**, e1601459 (2017).
- [49] C. Jin *et al.*, *Nature (London)* **567**, 76 (2019).
- [50] K. Tran *et al.*, *Nature (London)* **567**, 71 (2019).
- [51] Y. Cao, V. Fatemi, S. Fang, K. Watanabe, T. Taniguchi, E. Kaxiras, and P. Jarillo-Herrero, *Nature (London)* **556**, 43 (2018).
- [52] G. Chen *et al.*, *Nat. Phys.* **15**, 237 (2019).